Drive of parallel flows by turbulence and large-scale E x B transverse transport in divertor geometry

D Galassi, Patrick Tamain, Hugo Bufferand, G Ciraolo, Philippe Ghendrih, C Baudoin, C Colin, Nicolas Fedorczak, N Nace, E Serre

Drive of parallel flows by turbulence and large-scale $E \times B$ transverse transport in divertor geometry

D. Galassi[1], P. Tamain[2], H. Bufferand[2], G. Ciraolo[2], Ph. Ghendrih[2], C. Baudoin[2], C. Colin[1], N. Fedorczak[2], N. Nace[2] and E. Serre[1]

[1] *Aix Marseille Université, CNRS, Centrale Marseille, M2P2 UMR 7340, 13451, Marseille, France*

[2] *IRFM, CEA Cadarache, F-13108 St. Paul-lez-Durance, France*

e-mail address: davide.galassi@univ-amu.fr

Abstract

Poloidal asymmetries of parallel flows in edge plasmas are investigated by the 3D fluid turbulence code TOKAM3X. A diverted COMPASS-like magnetic equilibrium is used for simulations. Measurements and simulations of parallel Mach numbers are compared and exhibit good qualitative agreement. Small-scale turbulent transport is observed to dominate near the Low Field Side midplane, even though co-existing with significant large-scale cross-field fluxes. Despite the turbulent nature of the plasma in the divertor region, simulations show a low effectiveness of turbulence for the cross-field transport towards the Private Flux region. Nevertheless, a complex pattern of fluxes associated to the average field components, are found to cross the separatrix in the divertor region. Large-scale and small-scale turbulent $E \times B$ transport, along with the ∇B drift, drive the asymmetries in parallel flows. A semi-analytical model based on mass and parallel momentum balances allows one to evaluate the poloidal drifts effects on the asymmetry pattern. As in experiments, a reversed B_T simulation provides

a way to separate self-consistently the effects of turbulent transport and the large-scale flows, that must reverse for a reversed field. The large-scale contribution is found to be responsible for typically the 50% of the effect on the Mach number, evaluated at the top of the machine. The presented picture shows a complex interplay between drifts and turbulence, underlining the necessity of a global approach in the edge plasma modelling including the self-consistent turbulence description.

Keywords: Poloidal asymmetries, Turbulence, Divertor geometry, Large-scale flows

1 Introduction

A widely known feature of tokamaks is the poloidal asymmetry of the parallel flows in the Scrape-Off Layer (SOL), found experimentally on multiple machines[1]. These asymmetries are relevant for the tokamaks operation, since they cause imbalances in the heat flux deposition on targets, and locally change the SOL width. Moreover, the induced plasma rotation in the SOL is believed to influence the cross-field transport at the separatrix, and thus the overall confinement. Lastly, the plasma fluxes affect the neutral recycling and the impurity transport.
The parallel flow in the open field lines region appears to be directed towards the inner target on a wide poloidal span in the SOL, with Mach number values close to 0.5 at the top of the machine. Parallel flows are triggered by multiple mechanisms. First of all, the presence of a divertor target (or a limiter), which drives large poloidal flows in the SOL in its vicinity. Secondly, all the sources of particles and momentum can alter this equilibrium. Turbulent transport across the separatrix represents an important source of particles and momentum for the SOL. Along with this, other elements that can alter the global equilibrium of the SOL are the large-scale drifts. Numerical simulations with 2D transport codes including drifts can qualitatively recover the right trends for the fluxes in the SOL [2]. However, 2D transport codes have the tendency to underestimate quantitatively the magnitude of the parallel flow directed towards the inner target. An imposed ballooning on transport coefficients, with a dependence on $1/B_T$, enhances the parallel flux towards

the High Field Side (HFS), and an additional radial pinch velocity is added in some cases in order to quantitatively match the results [3].
Turbulent transport is known to strongly impact the particle and energy transport across the flux surfaces, in particular near the Low Field Side (LFS) midplane. Turbulence is thus an important source of poloidal asymmetries in the SOL, as it has been experimentally verified, for example, on Tore Supra[4]. Large-scale drifts co-exist with small-scale turbulence among the transport mechanisms, and their effects can superpose in a complex pattern. In order to catch these phenomena and their interactions it is useful to address the problem with a first principle turbulence code.
A great international effort is ongoing in the community of plasma edge turbulence, focused on the development of the simulation tools. Among the others, we have the 3D turbulence codes BOUT++[5], GBS[6], HESEL[7] and TOKAM3X[8]. Some differences exist in the physical model underneath each of these codes. BOUT++, for example, is a framework able to include different physical terms in the equations, among which the energy conservation, electro-magnetic effects and even kinetic effects. BOUT++ users have recently investigated the blob dynamics in the SOL, limiting the analysis to a flux tube geometry (see [9] and [10]). Another series of BOUT++ application is focused instead on electro-magnetic phenomena, as for example the ELMs dynamics (see [11],[12],[13]). GBS as well includes important physical features, as the description of the neutral dynamics, electro-magnetic effects and the evolution of the species temperatures, though usually not all these elements are included in the simulations at the same time. Recent studies have been carried out on the global flows driven by turbulence in 3D simulations with GBS (see [14],[15]) in a non-isothermal framework, using a limiter configuration. The HESEL code has been recently dedicated to the analysis of the L-H transition [7], making use of a simplified geometry. It is useful to remind the existence of other types of simulation tools, as the gyrokinetic particle-in-cell code XGC1[16], which could address, in principle, the subjects of this paper, taking into account a realistic diverted geometry with both open and closed field lines. However this type of code remains extremely costly in terms of computational time. The work presented in this paper is aimed at understanding the driving of parallel flows by turbulent transport and large-scale flows, in the framework of a realistic X-point geometry. Despite the fact that this magnetic configuration is the most widely used in present and future tokamaks, including ITER, many aspects of the physics related to the divertor are still not fully understood. One of these

aspects is the effect of the particular diverted geometry on the turbulent transport. Still a little knowledge is available on the turbulence in the vicinity of the X-point and in the divertor region, where turbulence may have a significant role for the spreading of the heat flux on the divertor targets[17]. We present in this paper the results obtained with the 3D fluid turbulence code TOKAM3X which, despite a simpler physical model with respect to the above-mentioned codes, can simulate plasma scenarios in complex magnetic configurations as the diverted one[8], taking into account both closed and open field lines. Old versions of the TOKAM3X code have been used before to inspect the role of the turbulent transport in the driving of parallel fluxes (see [18],[19]) in a limiter magnetic geometry, showing the necessity of the description of the edge turbulence for the build-up of poloidal asymmetries. Nevertheless, the recent developments of TOKAM3X allow us to give a deeper insight on the driving of parallel flows in the SOL in a realistic 3D magnetic equilibrium, underlining the role of the peculiarities of a diverted magnetic configuration, as the presence of the Private-Flux Region or the poloidal inhomogeneity in the flux expansion. In this framework, we aim at understanding at a fundamental level the basic physical mechanisms causing the build-up of poloidal asymmetries in parallel fluxes, identifying self-consistently the respective contributions of small-scale turbulence and large scale flows.

2 The TOKAM3X code

The results presented in this paper are obtained with the TOKAM3X code. TOKAM3X is a 3D fluid turbulent code for the tokamaks plasma edge simulation. The physical domain extends from the closed flux surfaces in the vicinity of the separatrix to the open flux surfaces. In the last years, TOKAM3X has been developed in order to handle complex magnetic configurations, including the divertor geometry. In this paper we will discuss mostly of the simulations in divertor configuration, even if some of the considerations that will be made are not restricted to this particular geometry.
TOKAM3X solves a set of drift-reduced conservation equations for mass, parallel momentum, electric charge and energy for electrons and ions, in an electrostatic approximation. In TOKAM3X turbulence arises spontaneously, caused mainly by the interchange instability, when a critical value for the

radial pressure gradient is reached. It is a flux-driven turbulent code, without any time nor space scale separation. This means that in the code, a large spectra of fluctuations is taken into account, and the interplay between different scales is treated self-consistently, by means of the non-linear terms. Simulations are pushed until they reach a pseudo-equilibrium, namely a state in which the fields averaged over the toroidal direction are constant (or nearly constant) in time.
The following normalized set of equations describes the time evolution of the electron density N, the ion parallel momentum Γ, the parallel current $J_\parallel$ and the electrostatic potential Φ:

$$\partial_t N + \vec{\nabla}\cdot\left(\left(\Gamma - J_\parallel\right)\vec{b} + N\vec{u}_E + N\vec{u}^e_{\nabla B}\right) = D_N\nabla^2_\perp N + S_N \quad (1)$$

$$\partial_t \Gamma + \vec{\nabla}\cdot\left(\Gamma^2/N\vec{b} + \Gamma\vec{u}_E + \Gamma\vec{u}^i_{\nabla B}\right) = -2\nabla_\parallel N + D_\Gamma\nabla^2_\perp\Gamma \quad (2)$$

$$\partial_t W + \vec{\nabla}\cdot\left(W\Gamma/N\vec{b} + W\vec{u}_E + W\vec{u}^i_{\nabla B}\right) = \vec{\nabla}\cdot\left(N\left(\vec{u}^i_{\nabla B} - \vec{u}^e_{\nabla B}\right)\right) + \vec{\nabla}\cdot\left(J_\parallel\vec{b}\right) + D_W\nabla^2_\perp W \quad (3)$$

$$N\nabla_\parallel\Phi - \nabla_\parallel N + \eta_\parallel N J_\parallel = 0 \quad (4)$$

A quasi-neutrality assumption is made, leading to the equality of the ion and electron densities: this hypothesis is justified since the mesh grid is much larger of the typical Debye length for the plasma edge. At the present moment the code is run in isothermal mode, with a constant temperature for both species, $T_e = T_i = T_0$, where T_0 is the reference temperature. In the normalized equations, by consequence, temperature has a constant unitary value and so the ion static pressure corresponds with the ion density. In these equations, the vorticity W is calculated with a Boussinesq-like approximation [20], so it can be defined as

$$W = \vec{\nabla}\cdot\left(\frac{1}{B^2}\vec{\nabla}_\perp\Phi + \frac{1}{B^2 N}\vec{\nabla}_\perp(NT_i)\right) \quad (5)$$

If compared to the physical model presented in [19] or [21], where T_i was set to 0 in the vorticity definition, the new version of the code drops the hypothesis of cold ions, taking into account their pressure.
The electric drift velocity is calculated as $\vec{u}_E = (\vec{B}\times\vec{\nabla}\Phi)/B^2$, while the

curvature drift velocity is expressed as $\vec{u}_{\nabla B}^{i/e} = \pm 2T_{i/e}(\vec{B} \times \vec{\nabla} B)/B^3$, with the sign + for the ions i and − for the electrons e. This formulation of the curvature drift takes into account the diamagnetic cancellation, and conserves the divergence of the particle flux associated to the diamagnetic drift.
Two main limitations exist in the presented version of the code. The first one is the absence of a model for neutral dynamics, that is known to deeply affect the SOL physics. From this point of view, TOKAM3X has been recently coupled with EIRENE[22], but the results of the coupled version are still under investigation and go beyond the scope of this paper. The second limitation consists in the isothermal run mode. Though the code includes the possibility to solve the energy conservation equations for ions and electrons, the isothermal mode is mostly used for computational time constraints. By consequence some physical mechanisms as the thermo-electric currents, which are linked to the temperature gradients in the parallel direction and could play an important role in the setting of the poloidal asymmetries, and are hence neglected. For these reasons, the results of the presented simulations are consistent to plasma conditions close to the sheath-limited regime, where temperature is poloidally constant and the neutral dynamics should play a more limited role. In addition, the electro-magnetic effects are neglected under the hypothesis of low-beta plasma: therefore only L-mode plasmas can be simulated.
The whole TOKAM3X physical model is based essentially on four parameters. Three of them are diffusion coefficients, for density, parallel momentum and vorticity, and are set for the simulation as $D_{N,\Gamma,W} = 0.5 \cdot 10^{-2} \rho_L^2 \omega_c$, being ρ_L the ion Larmor radius and ω_c the ion gyrofrequency. These coefficients act as filters for the small-scale perturbations, of the order of the Larmor radius. The imposed values should be sufficiently low to ensure a negligible impact of diffusive transport if compared to turbulence and advection by drifts. The last parameter is the parallel resistivity, that is set to $\eta_\parallel = 1 \cdot 10^{-5} \frac{B_0}{en_0}$, where n_0 is the reference density used for the normalization.
Since the code does not deal with the neutral dynamics and is run in isothermal mode, ionization sources are not calculated self-consistently. Nevertheless, a particle source is imposed at the inner boundary of the geometrical domain, in the closed flux surfaces region, in order to mimic an ionization source poloidally distributed over the edge region. The behaviour of the system is therefore closer to a sheath-limited regime, where the main part of the neutrals ionizes in the edge region, than to an high-recycling regime, in which

the ionization source would be mainly localized close to the divertor targets. The imposed particle source has a Gaussian shape in the radial direction, with a half-width of about $a/16$, where a is the minor radius. The particle source is constant along the poloidal and the toroidal directions. Bohm's boundary conditions are used at the target plates in the parallel direction, while Neumann conditions are imposed in the radial direction on the closed flux surfaces inner boundary and on the open flux surfaces outer boundary. The TOKAM3X grid resolution is of the order of the main normalization length, that is the ionic Larmor radius. The minor radius of the simulated tokamak measures 256 ρ_L, and the aspect ratio is 2.8. A COMPASS-like diverted geometry is used, since it has a suitable size for the simulations. A future comparison with experimental results from this device is envisaged, as its diagnostic system is appropriate for an investigation on the presented results [23].
Figure 1 shows the mesh grid used for the simulations, and a snapshot of the density fluctuations.

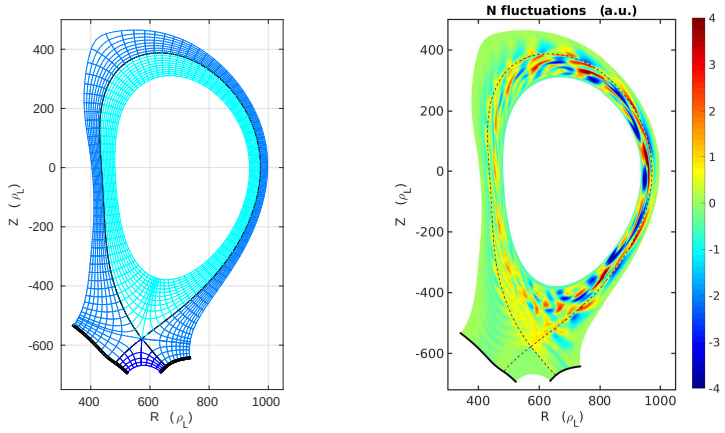

Figure 1: Left: COMPASS-like mesh grid used for TOKAM3X simulations. Displayed grid is coarser than the actual used by the code by a factor four, both in radial and poloidal direction. Right: Snapshot of a poloidal section showing the density fluctuations at a specific timestep.

3 Large-scale flow equilibrium in divertor simulations

The Mach number distribution is frequently used for the characterization of the parallel flows in the SOL. This quantity is defined as the ratio between the velocity in the parallel direction and the acoustic velocity $M = u_{\parallel}/c_s$, with $c_s = \sqrt{(T_e + T_i)/m_i}$. Multiple experimental measurements have been done on this quantity, representing a solid basis for a comparison with numerical results. The parallel Mach number resulting from the turbulent simulations in COMPASS-like geometry, averaged in time and toroidal direction, is shown in figure 2a for different radial positions in the SOL.

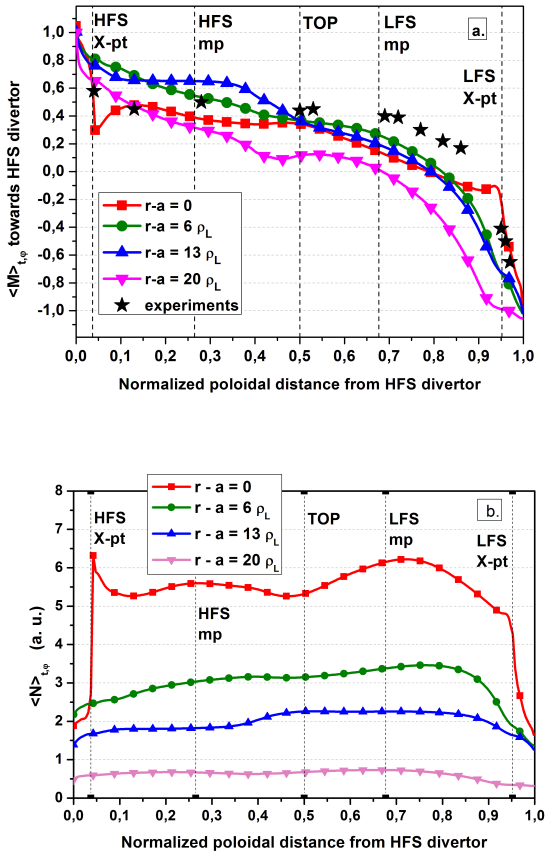

Figure 2: a) Poloidal profile of the parallel Mach number, taken at different flux surfaces in the SOL. Radial distance from the separatrix at the LFS midplane of each flux surface is indicated by the quantity $r - a$. Vertical dashed lines represent, from left to right, the location of the X-point at the HFS, the HFS midplane, top, LFS midplane and the X-point at the LFS. Experimental points are taken from [1]. b) poloidal profile of the ion density averaged in time and toroidal direction

As one can notice from figure 2a, the poloidal profile of the Mach number shows some common features with the multi-machine experiment presented in [1]. In particular two important experimental features are reproduced: a Mach number of $M \simeq 0.35 - 0.4$ is found at the top of the machine, and the stagnation point is located between the X-point and the Low-Field Side midplane. These characteristics are more evident for the flux surfaces close to the separatrix, while for flux surfaces further out in the SOL the Mach number profile is more poloidally symmetric.
In our simulation, the total plasma pressure, $\Pi = N(T_e + T_i)(1 + M^2) = 2N(1 + M^2)$ in the isothermal hypothesis, is almost constant on a flux surface for the main Scrape-Off Layer region. One can thus qualitatively relate the Mach number poloidal distribution with the density one, shown in figure 2b. The topological discontinuity introduced by the X-point strongly affects the plasma flow for the first flux surfaces outside the separatrix. The presence of the PFR, indeed, causes a drop in density along the field lines in the divertor region. Large poloidal density gradients are visible in figure 2b in the divertor region for approximately the first 10 Larmor radii outside the separatrix. By consequence, the plasma accelerates in the parallel direction, to compensate the loss in static pressure. At the X-point in the HFS, a small density accumulation is found, with a correspondent deceleration in the parallel flow. This density accumulation is probably triggered by the presence of the topological discontinuity introduced by the X-point. The mechanisms transporting particles to this region will be analyzed in section 4. This effect is however limited to the first flux surfaces outside the separatrix, while further out in the SOL, density decreases smoothly going towards the inner target, and we find elevated, nearly sonic, parallel flows in the region between the HFS midplane and the HFS divertor.
The parallel Mach number can be also seen as a global index of the cross-field transport across the separatrix. In a steady-state regime indeed, considering a constant total pressure in the main SOL region, and excluding any supersonic transition in the simulated domain, we have:

$$\frac{dM}{dx_\parallel} = \frac{1 + M^2}{1 - M^2} \frac{S}{N c_s} \tag{6}$$

Where $x_\parallel$ is the parallel coordinate and S is the particle source. This simple equation shows that the parallel gradient of the Mach number, and so also the the poloidal gradient, has the same sign of the particle source. In our

simulation, in particular, we find monotonically increasing Mach number profiles, with the exception of the above-mentioned region around the X-point, meaning a positive particle source distributed along the SOL. Even if in our model the ionization source in the SOL is neglected, parallel flows are driven in this region by several transport mechanisms, such as large-scale drifts, diffusion or small-scale turbulence. One must keep in mind, however, that the hypothesis of constant total pressure is reductive, and that the parallel Mach number is the result of a complex equilibrium between the transport of particles, parallel momentum and energy in the perpendicular and parallel directions. A more detailed method for the Mach number calculation can be found in [24]. In order to better explain the parallel Mach number profiles we thus need to have a global view of the main cross-field fluxes that participate in the determination of the SOL equilibrium. We are interested, in particular, in distinguishing the role of turbulent fluxes from the large-scale flows caused by drifts.

4 Mean-field and fluctuating components of $E \times B$ cross-field fluxes

As a first step in the understanding of the effect of turbulence on the complex SOL equilibrium, we analyze the cross-field fluxes which come into play, trying to separate a fluctuating part from the steady-state one in the background. An important term that is inspected is the flux associated to the electric drift in the direction perpendicular to the flux surfaces. In a generalized coordinate system, we call ψ this direction, that also identifies the flux surface coordinate. In a tokamak with circular cross-section, this direction would coincide with the radial one. An averaging operation in the toroidal direction and in time on the $E \times B$ flux leads to:

$$< N u_E^{\psi} >_{t,\varphi} = < N >_{t,\varphi} < u_E^{\psi} >_{t,\varphi} + < \tilde{N} \tilde{u}_E^{\psi} >_{t,\varphi} \tag{7}$$

Where $\tilde{X} = X - < X >_{t,\varphi}$ is the fluctuating component of a generic field. The first term on the right-hand side is thus associated to the averaged components of the fields and will thus be referred to, from now on, as *mean-field flux*, while the second term on the right-hand side will be called *fluctuating flux*. This analysis can only be done as a post-processing, since TOKAM3X

does not make any scale separation. Since the micro-turbulence, characterized by big wave numbers, can interplay with large-scale fluctuations, the mean-field component is not necessarily associated only to the drifts, but keeps a trace also of an average contribution of turbulence, through the equilibrium of density and potential driven by the latter. In order, then, to isolate the contribution of turbulence to the cross-field transport, we will need to use an approach inspired by the experiments, described in section 7. If we make the separation explained in (7) a posteriori, however, we can distinguish a mean-field and a fluctuating part that could give as a first idea at least on the localization and the relative order of magnitude of the turbulence and the large-scale drift processes. Simulation results for $E \times B$ cross-field transport are reported in figure 3.

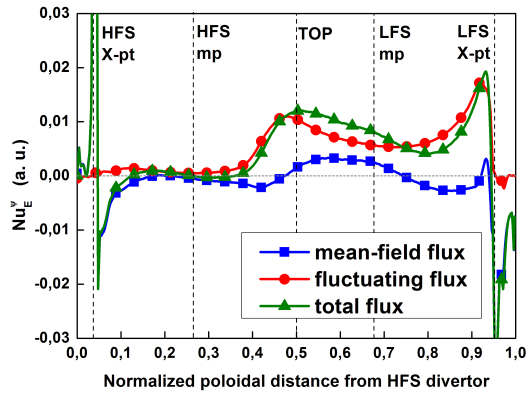

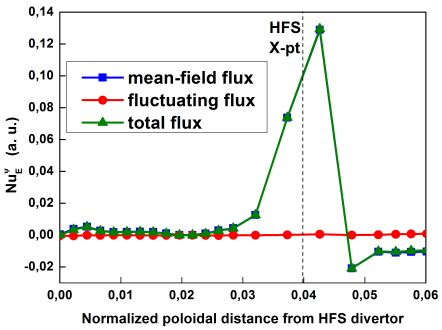

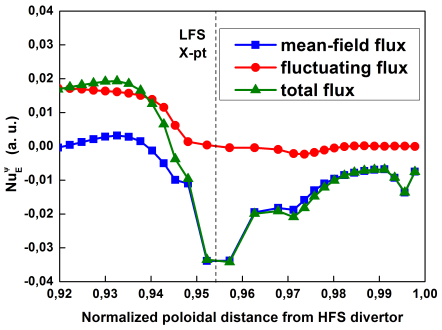

Figure 3: a) Poloidal profile of mean-field, fluctuating and total $E \times B$ cross-field flux at the separatrix in the direction perpendicular to flux surfaces. A positive quantity represents a flux directed radially outwards. b) Zoom on the HFS divertor region. c) Zoom on the LFS divertor region

We can notice in figure 3a that, as expected, the fluctuating transport associated to the $E \times B$ drift is located mainly in the LFS, while it is nearly absent in the HFS. This feature has been already found experimentally ([4],[25]), and it confirms clearly that the interchange is the predominant instability mechanism. Instead, the mean-field flux appears to be the stronger mechanism in the vicinity of the X-point at the HFS and in the divertor legs. We can see that at the Low Field Side the mean-field component of the flux has a non-negligible importance with respect to the fluctuating one. We can also notice that the mean-field flux changes its direction at a position located slightly lower than the LFS midplane. This particular shape can be explained easily considering the electric potential behaviour in the SOL. Since the electrons are quasi-adiabatic, the electric potential gradient in the parallel direction tends to follow the one in density. We have thus the build-up of poloidal electric fields, that causes a significant radial transport by $E \times B$ drift. The change in the radial direction of the flux reflects the changing in sign of the poloidal gradient of the electric potential, which peaks, at the separatrix, poloidally close to the LFS midplane. This position, as suggested before, coincides also with the density poloidal peak, as one can see in figure 2b. The peak in the density poloidal distribution at the LFS midplane is likely to be determined, at least partly, by the small-scale turbulence cross-field transport. This peaking becomes less evident going radially outwards in the SOL, where turbulence is weaker. This effect has already been found with other fluid turbulence codes[14], and can be better understood with the analysis shown in section 6.

Mean-field fluxes show pronounced peaks also at the X-point location. These fluxes are probably triggered by the particular topology associated to the diverted configuration. At this location indeed, gradients in poloidal directions are strong, since the Private Flux Region (PFR) tends to act as a plasma sink. By consequence, in our simulations, an $E \times B$ flux crosses the separatrix at the divertor LFS, and passing through the Private Flux Region can arrive at the HFS, affecting the HFS Scrape-Off Layer in the vicinity of the X-point. Looking at figure 3b and 3c, the mean-field $E \times B$ flux is indeed negative in the LFS, and positive at the HFS around the X-point. By consequence, a small density accumulation is seen only at the HFS, corresponding to a low Mach number, as visible in figures 2a and 2b. The inward flux visible between the HFS X-point and the HFS midplane is again caused by the poloidal gradient, which is associated to the density accumulation.

Unexpectedly, the fluctuating flux seems not to be peaked at the LFS mid-

plane. Instead, it shows two peaks located at the top and at the LFS X-point. Also the mean-field flux seems to be greatly enhanced in the X-point region. These data must be read, however, taking into account the particular geometric effects linked to a realistic diverted geometry. Indeed, as visible in figure 1, the mentioned positions correspond to the poloidal locations where the poloidal field is minimum on a flux surface, so also where the flux expansion is more pronounced. This suggests that fluxes across the flux surfaces adapt in order to be larger when flux expansion is larger. An explanation to this self-organization behaviour can be given as follows. The parallel transport tends to homogenize the plasma structures on a flux surface, damping the majority of the cross-field fluctuations, and keeping the ones with a lower parallel wave number. For this reason, the perpendicular transport tends to adapt its behaviour according to the local flux expansion, resulting in stronger fluxes where further flux surfaces must be reached in order to keep the turbulent structures almost field-aligned. So, despite the fact that in the model gradients are calculated in the physical space, taking into account the full metrics, the reference space for turbulent transport is not the physical space, but, instead, the one defined by the magnetic field. This geometric effect partially hides the real poloidal distribution of the effectiveness of the turbulent transport. Indeed, we are not strictly interested in the position where the cross-field fluxes are stronger. Instead, we aim at understanding how far in the magnetic space mass and momentum can be transported. In order to find the position where the cross-field transport is more effective so, one should divide the flux values by the local flux expansion. This quantity can be defined as:

$$f_x\left(\psi,\theta\right)=\frac{\left|\vec{\nabla}\psi_{mp}\left(\psi\right)\right|}{\left|\vec{\nabla}\psi\left(\psi,\theta\right)\right|} \tag{8}$$

Where θ is the angular coordinate on the poloidal plane and the subscript mp indicates that the quantity is calculated at the LFS midplane. Figure 4 shows the $E\times B$ fluxes weighted by the flux expansion.

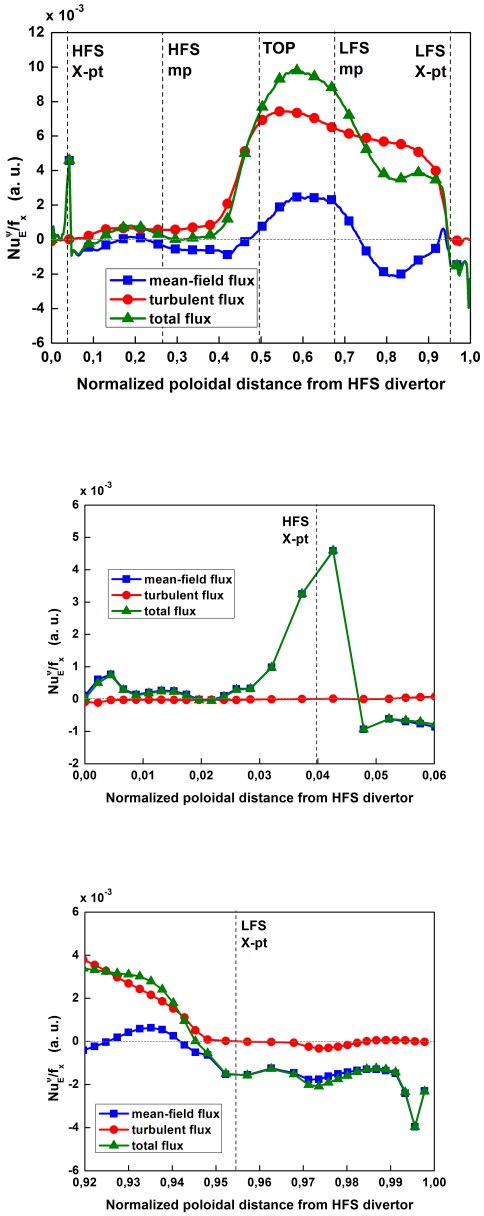

Figure 4: a) Poloidal profile of mean-field, fluctuating and total $E \times B$ cross-field flux at the separatrix, divided by the flux expansion f_x referred to the midplane.b) Zoom on the HFS divertor region. c) Zoom on the LFS divertor region.

One can see that, as expected, the turbulent cross-field transport is peaked near the LFS midplane, where the interchange instability process is stronger. The small deviation from the exact peaking at LFS midplane is probably due to complex non-linear mechanisms which can locally alter the perpendicular transport in the vicinity of the separatrix. These phenomena will be introduced in section 7. Regarding the comparison between mean-field and fluctuating components, figure 4 still suggests that turbulence is the main mechanism that allows particles to cross the flux surfaces, independently from their compression. While the flux expansion geometric effect on the fluctuating flux is evident by figure 3, the mean-field fluxes do not seem to be distorted by this geometrical feature. We still find indeed the sinusoidal flux shape at the LFS, an inward flux at the LFS in the divertor region and a positive outflux at the X-point in the HFS. Nevertheless, the amplitude of the fluxes in the vicinity of the X-point is drastically reduced, since the flux expansion has the larger values in this region. This suggests that the geometrical effect of flux expansion should be valid also for the mean-field fluxes. However our physical explanation, which involves the alignment of the structures along the field lines, can be applied to the small-scale fluctuations, and could be identified as a linear effect. In order to verify its validity also for the mean-field fluxes, a non-linear analysis would be required, since it would involve the interaction between small-scale and large-scale structures. Moreover, beside this geometrical effect, the flux expansion and the topological discontinuities introduced by the X-point, could modify the transport properties, affecting the equilibrium and so also the mean-field fluxes. For this reason, more simulations are needed to check the flux expansion effect on mean-field fluxes, with a limiter geometry which would include a controlled flux expansion while excluding the topological effect of the X-point.
The pattern of the poloidal $E \times B$ flux in the SOL simply derives from the radial electric potential gradient. Since this gradient points towards the separatrix, the $E \times B$ poloidal flux in the SOL is directed towards the outer target, as it was expected. On the contrary, for the closed field lines the $E \times B$ poloidal flux is oriented in the counterclockwise direction, implying a strong shear at the separatrix that probably affects the turbulent transport. In the Scrape-Off Layer the $E \times B$ poloidal flux is found to peak at the LFS midplane. This is partly due to the peaking in density at the midplane, and partly to the $1/B$ dependency of the drift, which makes the drift velocity amplitude increase with the major radius.

5 Turbulence and flows in divertor region

In the divertor region, in the proximity of the separatrix, a complex equilibrium takes place. The presence of the Private Flux Region causes strong radial particle and momentum losses, by $E \times B$ drift and diffusion. We can see an inward radial flux in figure 4c for the outer leg. We also observe that this cross-field flux is entirely associated to the mean fields. Indeed, it is caused by a poloidal density gradient, clearly visible in figure 2b, and it develops with the same process as described in section 4. The radial particle and momentum fluxes contribute to the build-up of the poloidal density gradients in the divertor region in a time-evolving process, until an equilibrium is reached.

In our case, drifts transport particles (and momentum) from the SOL to the PFR on the LFS and vice-versa for the HFS. On the outer leg of the divertor, the flux goes from a zone at high density, the SOL, to a zone of low density, the PFR. The cross-field transport is thus more efficient on the outer side if compared to the inner one, where, on the contrary, it is directed from the PFR to the SOL. We must recall here, however, that our model is isothermal: the dynamics of neutrals, and so the different divertor regimes, can alter or even inverse the direction of the poloidal density gradients in proximity of the targets, and, by consequence, also the radial drifts.

This complex flux pattern has already been put in evidence by 2D transport codes with drifts [26]. With our code we can evaluate, in addition, the combined effects of topology and turbulence on the edge plasma equilibrium. It is interesting to inspect, in particular, the role of turbulence in the vicinity of the X-point.

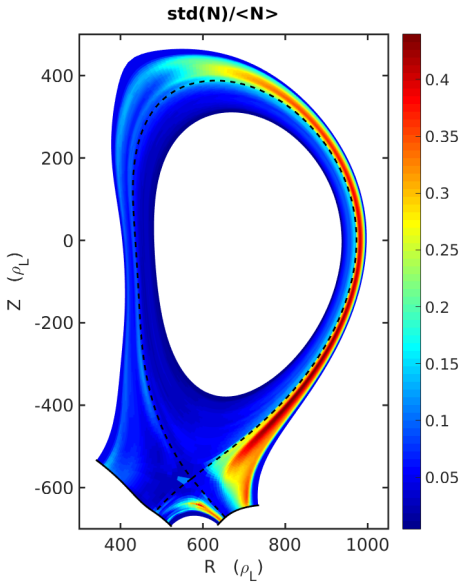

Figure 5: Poloidal map of standard deviation of density fluctuations compared to the local density value, averaged on time and toroidal direction.

Figure 5 shows the poloidal distribution of the density fluctuations in the simulated domain. As one can expect, density fluctuations are mainly localized at the LFS midplane. Filaments propagate from the closed flux surfaces to the SOL around the LFS midplane region. Then, they are transported down towards the divertor, while propagating also radially. In the vicinity of the X-point, they assume an elongated shape in the radial direction: this is likely to be due to the big flux expansion at the X-point. In the thin region around the outer divertor leg, that has a thickness of about 10 Larmor radii, they tend to progressively disappear. There are different potential causes for this behaviour. First of all, near the separatrix, the connection length between the region below the X-point and the LFS midplane, where the fluctuation amplitude has its maximum, is long if compared to the rest of the SOL. This disconnection can facilitate the damping of small scale turbulence by, for example, collisional mechanisms. For flux surfaces further out from the separatrix, the connection length is lower, and indeed fluctuations appear to be less damped. Secondly, the conditions in this region are not favourable for the development of the interchange instability, which requires pressure and magnetic field gradients to be aligned. In our simulations, the radial density profile shows a shape similar to the one described by [27] and found by the 2D transport codes [26]. In the vicinity of the separatrix, the radial density gradient is small or it can even be directed outwards, so the interchange instability can be inhibited. Further out in the SOL, the conditions suitable for the instability development are re-established. The relative weight of these processes on the fluctuation damping is still to be determined and require further analysis.

The Private Flux Region is shown to be turbulent, in agreement with what has been recently found experimentally on MAST [28]. In our simulations, the density structures appear to enter radially in the PFR from the Scrape-Off Layer, being then suddenly damped. The presence of density and electric potential fluctuation in the PFR does not imply in this case an efficient turbulent particle transport towards the PFR. Indeed, since the oscillations of these two fields are not in phase at this point, the turbulent flux, as defined in (7), is close to zero even if the plasma is turbulent. Nevertheless, mean-field flux towards the PFR is found, as we can notice in figure 4. It is important to recall that we are here solving an isothermal physical model so we are excluding some potential instability mechanism generated by the temperature gradients, that could affect the plasma dynamics in PFR [17].

Globally, the presence of the divertor is found to change significantly the

overall plasma equilibrium, in particular with the creation of strong poloidal density gradients between the targets and the X-point. At the steady-state, however, as visible in figure 4, the radial $E \times B$ flux magnitude towards the Private Flux Region is still far smaller than the outflow at the midplane, so its impact on the parallel flux in the SOL should be limited. This fact can be checked with the numerical simulation described in section 7, that deals with the inversion of the toroidal field.

6 Driving of SOL parallel flows by ballooned transport and drifts

We have now more elements to analyze the Mach number poloidal profiles. In this section we try to evaluate the different contributions which drive the asymmetry in parallel fluxes shown in section 3.

6.1 Poloidal distribution of parallel flow sources

Let us recall the simple model proposed by Gunn et al.[4]. Considering a constant dynamic pressure along the field line, and solving the particle and parallel momentum balance in absence of external sources of momentum, one can express the parallel Mach number in function of the particle source distribution along the field line, as follows:

$$\frac{M}{M^2+1} = s_{\parallel} - \frac{1}{2} \tag{9}$$

Where $s_{\parallel}$ is defined as:

$$s_{\parallel} = \frac{1}{< S > L} \int_{-L/2}^{L/2} S \quad \mathrm{d}x_{\parallel} \quad , \quad < S >= \frac{1}{L} \int_{-L/2}^{L/2} S \quad \mathrm{d}x_{\parallel} \tag{10}$$

Where $x_{\parallel}$ is the curvilinear parallel coordinate, L is the total connection length, and S is the generic particle source term. In the SOL, where no ionization source is accounted for by our code, particles are brought by transport mechanisms, as the small scale turbulence and by large-scale outflows from the edge region. Basically, we can describe this particle source

by taking to the RHS of equation (1) the divergence of the drift advection terms. Equation (9) shows that the stagnation point, namely the location where the parallel Mach number is null, equals the position along the field line where the particle source has its center of mass. We need to understand, thus, where the main source of particles for the parallel flow is located in the poloidal direction. Figure 6 shows schematically the main particle sources found in the SOL.

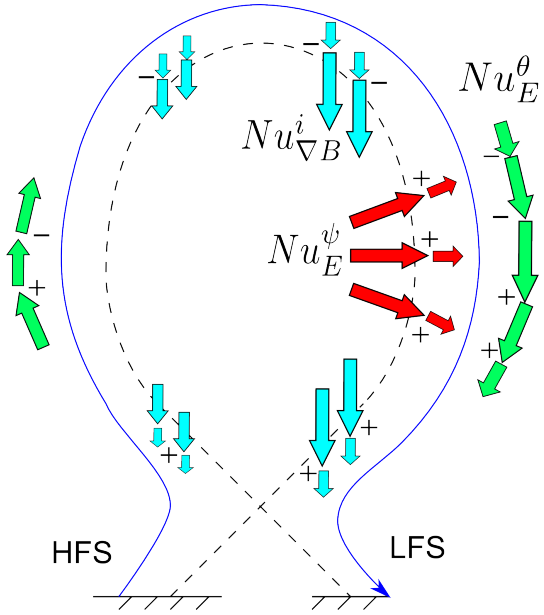

Figure 6: Poloidal distribution of particle sources in the SOL. Arrows length are qualitatively proportional to the correspondent flux amplitude. The signs plus and minus indicate respectively a positive or a negative source for the parallel flux, and they are located at the position where these sources appear.

Figure 6 shows separately several contributions to the parallel flow. The first source mechanism that we inspect is the divergence of the $E \times B$ flux across the flux surfaces. As we have seen in figure 3, mean-field and fluctuating fluxes sum up in a total flux which is peaked around the LFS midplane, and it is generally spread over the majority of the LFS. This flux is found to be maximum near the separatrix in the radial direction, as expected from the fact that radial gradients are maximum at this position. The divergence of this flux is thus negative all along the LFS, constituting so a source for the parallel flow. On the HFS this source is almost null, as could be expected from the flux analysis in section 4. The small-scale turbulence, so, represents a strong source of in-out asymmetry. The second source term is related to the divergence of the poloidal component of the $E \times B$ advection velocity. This flux is directed towards the outer target, accordingly to the fact that the electric field is directed radially inward. Moreover, in our simulations, this flux is peaked at the outer midplane. This peaking implies a negative source for the parallel flow for the upper part of the LFS, and a positive source for the lower part of the LFS. On the HFS, this source has the same shape, but its magnitude is lower. Indeed in COMPASS geometry, the poloidal $E \times B$ velocity does not vary much along the HFS, since the major radius is quite constant in this region. Moreover, in our simulations the density profile is nearly flat in this region. Therefore, also this source is stronger for the outer SOL than for the inner SOL. The third source term is the divergence of the ∇B drift: this coincides with the divergence of the diamagnetic drift in the fluid approach. As illustrated in figure 6, this term represents a positive ion source in the lower side of the LFS midplane, and a negative one on the upper side. Also this source mechanism is weaker on the HFS, for the same reasons as the ones described for the $E \times B$ poloidal flux. Flows in parallel direction triggered by the divergence in the poloidal drifts are usually known as Pfirsch-Schlüter (P-S) flows. In absence of other mechanisms, they would lead to ion parallel flows with a cosine form along the poloidal direction, directed towards the top of the machine at the LFS midplane (see for example [29]). The resultant parallel flow would be almost symmetric, if one excludes the effects related to the toroidal geometry. In our model, the divergence of the $E \times B$ radial flow shifts significantly the overall source of parallel flow to the LFS. More specifically, we notice from figure 6 that the majority of the particle source is concentrated between the LFS X-point and the LFS midplane. This source is qualitatively similar to the one derived by the experiments in Alcator C-mod [30]. From equation (9) we

readily understand that this causes the stagnation point to set in this region. In the HFS region, where no significant flux crosses the separatrix, as shown in figure 4, the parallel flux towards the inner target is nearly constant, or it increases more smoothly. The elevated values for the Mach numbers at the HFS tend to compensate the inner-outer side asymmetry in the static pressure. In this region, the cross-field transport is almost null, so particles are transported nearly exclusively by the parallel transport, from the LFS to the HFS.

This particle source picture is consistent with a sheath-limited regime, but it could change significantly in the high-recycling regime. In that case, the ionization source would be mainly concentrated at the target plates, and a flatter Mach number profile is expected. In a high-recycling or detached regime a parallel return flow could still exist, as a response to an imbalance in the divertor pressure (see [31](Chapter 18),[32]). Nevertheless, experiments carried out in different machines and in different density regimes show similar qualitative behaviour, despite the fact that the relative weight of transport mechanisms and the ionization source could vary significantly with the plasma conditions. For Alcator C-mod, an explanation for this is suggested in [30], arguing that the plasma ionization source could be partially compensated by the radial fluxes associated with the main chamber recycling. We have pointed out here some physical features that could lead to a parallel flow pattern qualitatively similar to the experiments. The relative importance of these mechanisms with respect to the ionization source and the other phenomena related to the plasma-wall interaction remains an open question, and simulations with a more complex physical model are necessary to evaluate it.

Considering that the total plasma pressure is almost constant in the main SOL, one readily understand that plasma density peaks near the location of the stagnation point. Both turbulence and large-scale drifts have been shown to contribute to set this location between the LFS X-point and the LFS midplane. In order to disentangle the roles of these mechanisms in the setting-up of this asymmetric equilibrium, turbulence is excluded in the semi-analytic study presented in section 6.2, which is focused on the closed flux surfaces. In section 7 instead, the toroidal field inversion is used to separate the two contributions in a self-consistent way.

6.2 Drift effects on poloidal asymmetries in the closed flux surfaces

The fluid drifts associated to the mean-fields are typically mechanisms that can alter the poloidal asymmetry in the tokamak, superposing their effects to the fluxes caused by turbulence. In order to isolate the role of the drifts from turbulence, we have run a simulation with TOKAM3X in which turbulence is artificially suppressed. TOKAM3X has the possibility to run in axysimmetric mode: it acts this way as a standard 2D transport code. In this running mode, at each time step the fields are averaged in the toroidal direction, thus inhibiting the turbulence, that, by nature, is a three-dimensional phenomenon. The fluid drifts, however, are included in the model and so they actually participate as transport mechanisms. The simulation is run in a limiter geometry, with the aim of excluding any possible effect of the X-point. The results of this simulation show a density peaking at the LFS midplane for the closed flux surfaces. We remind that here turbulence is excluded, and the diffusive transport is poloidally homogeneous. This density peak must thus have a different origin, that we try to explain with a semi-analytical approach.
We reduce here the model solved by TOKAM3X in order to point out clearly the drift effects on parallel fluxes. In particular, we solve the particle and momentum balance in the closed field lines region, in absence of turbulent transport, but taking into account in a simplified way the fluid drifts. Analytical investigations have already been done on this subject ([14],[32]), with a similar approach but different underlying hypotheses. We would like here to point out the way in which the density and the parallel flows poloidal asymmetries are linked to each other.
Our reduced model is isothermal. We do not solve the electric current balance, but we consider instead a fixed, and poloidally constant, radial electric field. For a given flux surface, the steady-state and toroidally averaged conservation equations for ion density and momentum can be written as:

$$\begin{cases} \vec{\nabla} \cdot \left(\Gamma \hat{b} \right) + \vec{\nabla}_\perp \cdot (N \vec{u}_\perp) = 0 \\ \vec{\nabla} \cdot \left[\left(\frac{\Gamma^2}{N} + 2N \right) \hat{b} \right] + \vec{\nabla}_\perp \cdot (\Gamma \vec{u}_\perp) - 2N \vec{\nabla} \cdot \hat{b} = 0 \end{cases} \tag{11}$$

Where diffusion has been neglected and a flux surface placed sufficiently far from the ionization particle source has been considered. Since in the

closed flux surfaces region there are no losses in the parallel direction, we neglect the divergence in the radial direction. This hypothesis is acceptable if we place sufficiently far from the limiter. Eliminating the terms in the radial direction, we are left with a 1D problem in the poloidal direction.

$$\begin{cases} \frac{1}{Rr}\frac{d}{d\theta}\left(R\left(\Gamma\frac{B^\theta}{B}+Nu^\theta\right)\right)=0 \\ \frac{1}{R}\frac{d}{d\theta}\left(R\frac{B^\theta}{B}\left(\frac{\Gamma^2}{N}+2N\right)+R\Gamma u^\theta\right)+2N\frac{B^\theta}{B^2}\frac{d}{d\theta}B=0 \end{cases} \tag{12}$$

Where u^θ is the drift velocity projected on the poloidal plane:

$$u^\theta=\frac{B^\varphi}{B^2}\left(\partial_r\Phi+\frac{\partial_r P_i}{N}\right) \tag{13}$$

In this reduced model, we consider the radial gradients as known quantities, and constant in the poloidal directions. Thus u^θ is assumed to be known a priori, and its poloidal variation is caused only by its $1/B$ dependence on the magnetic field. This hypothesis would be more appropriate for the open flux surfaces, where the electric and diamagnetic drifts sum up, other than for the closed flux surfaces where they tend to substract. However, even if the analysis is carried out for the closed flux surfaces, the physical mechanism described by this model is valid also in the SOL.
The first equation in 12 represents the conservation of the poloidal particle flux. The quantity $\mathcal{G}=R(\Gamma\frac{B^\theta}{B}+Nu^\theta)$ is constant on a flux surface and it is considered here as a parameter. The poloidal particle flux in each flux surface is determined basically by any source of parallel momentum and by the perpendicular transport properties.
The system of equations reduces thus to a single ordinary differential equation with the density N as unknown:

$$\frac{dN}{d\theta}=\frac{\mathcal{G}^2N\frac{B}{B^\theta R^2}\frac{dR}{d\theta}+\mathcal{G}N^2\frac{B}{B^\theta}\frac{du^\theta}{d\theta}-2N^3\frac{B^\theta}{B}\left(\frac{dR}{d\theta}+\frac{R}{B}\frac{dB}{d\theta}\right)}{2\frac{B^\theta}{B}RN^2-\mathcal{G}^2\frac{B}{B^\theta R}} \tag{14}$$

This equation has been solved numerically with a fourth-order Runge-Kutta method, taking the values of the magnetic field from a realistic magnetic equilibrium.
Figure 7 shows the results for different values of the u^θ velocity at the LFS midplane, and a comparison with the values for the density field taken directly from the TOKAM3X code.

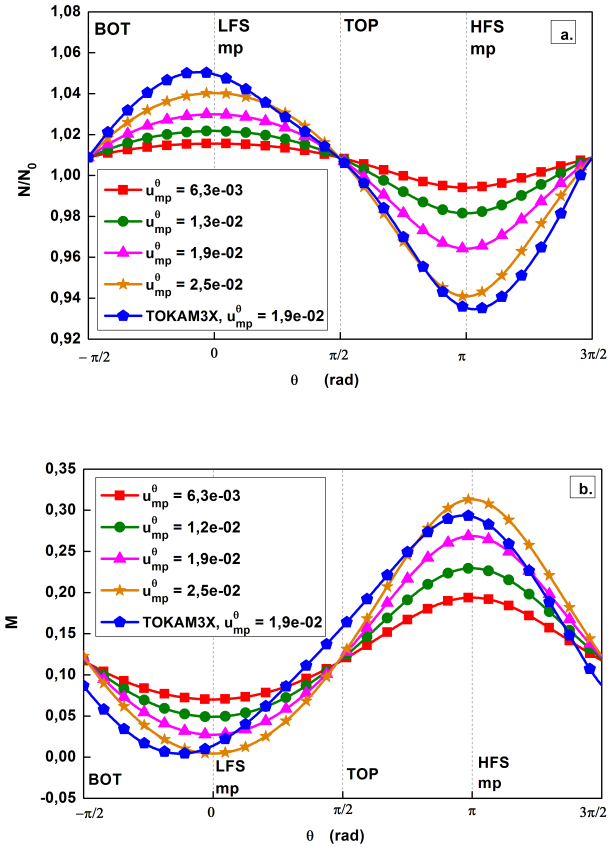

Figure 7: a) Poloidal profile of the toroidally averaged density, normalized to its mean value on the flux surface. The first curves are referred to the reduced model, with a variation of the drift velocity parameter. The last curve represents the data taken from the TOKAM3X axysimmetric simulation, with the associated poloidal drift velocity u^θ. On the abscissa, the poloidal angle expressed in radiants, where 0 indicates the LFS midplane position. In the TOKAM3X simulation, the limiter is at the bottom position (BOT). b) poloidal profiles of the parallel Mach number.

As we can see from the figure, the poloidal variation of the poloidal drift velocity drives an in-out density asymmetry on the flux surface, that increases when the poloidal velocity increases. In other words, a static mode $m = 1$ is found for the density and for the parallel flux, with the toroidal geometry amplifying the effects on the HFS.
Figure 7 shows that the reduced model well reproduces the results by the TOKAM3X code. The poloidal asymmetry of density is slightly underestimated by the reduced model when the poloidal drift velocity is comparable to TOKAM3X at the LFS midplane. This could be due to the fact that at the poloidal positions where, for example, the density is increased, also radial gradients are increased, with a consequent feedback on poloidal velocities and asymmetries. This non-linear effect is inherently related to the 2D nature of the problem, and so it can not be described correctly by the reduced mono-dimensional model. Moreover, in the TOKAM3X simulation the asymmetry between the inner and the outer side in the poloidal drift is actually stronger than the simple $1/B$ dependency. This semi-analytical model though allows us to better understand the mechanisms driving poloidal asymmetries in absence of turbulence. The divergence of the poloidal drift velocity is found to be the starting point for the poloidal asymmetry. In this particular case indeed, the variation of the poloidal drift with the major radius ($u^\theta \propto 1/B$) acts as a source of particles for the parallel direction, driving a plasma flow from the top to the bottom of the machine in the closed flux surfaces (and so in the opposite direction with respect to the Pfirsch-Schlüter flows in the SOL). The parallel flow driven in this way sums up with the one imposed by the boundary conditions. In our case, the mean parallel Mach number is positive for the whole poloidal angle as a result of the boundary conditions on the inner radial limit. The described P-S flow sums up with this imposed flow, implying a lower Mach number on the LFS and a higher one in the HFS. Since the total plasma pressure is almost constant on a closed field line the plasma density grows up in the LFS, while decreasing in the HFS. The poloidal asymmetry in density can further enhance the poloidal asymmetry, contributing to the poloidal divergence of the poloidal advection by the drifts.
This analysis shows that it is important to solve both particle and parallel momentum conservation when trying to predict the drift effects on the parallel Mach number. Indeed, a poloidal density cumulation has an immediate feedback on the parallel flows, and vice-versa. Being related to the poloidal variation of the drifts, this effect is more visible for tokamaks with small

aspect ratio. Even if this analysis is carried out for the closed flux surfaces, these considerations are valid also for the Scrape-Off Layer. In the SOL, the P-S parallel flow goes from the bottom towards the top. This flow sums up with the parallel flow driven by the presence of the sheath, which depends on the distribution of the outflow from the edge. In the TOKAM3X axysimmetric simulation, the observed density value is slightly larger at the LFS than at the HFS also for the open field-lines. However, the analysis of the poloidal equilibrium for the open field lines in the SOL is more complicated. Indeed Bohm boundary conditions at the targets intervene strongly, as well as the radial particle outflux from the edge region, driving parallel fluxes which superpose to the described ones. Fluxes in radial and poloidal directions are strictly coupled, and the divergence of the radial flux is no more negligible. The analytic study of the open flux surfaces case is left for a future work.
In turbulent simulations, the density asymmetry in the SOL is stronger than the effects found in axisymmetric simulations. This suggests that parallel flows caused by small-scale turbulence, co-existing with the P-S flows, intervene importantly in determining the LFS density peaking. Section 7 investigates the role of drifts and turbulence in the SOL with a method inspired by the experiments.

7 Impact of the inversion of toroidal field on global flows

We aim at distinguish the effects of turbulence and large-scale drifts on the cross-field transport. As explained before, this can not be done by the code itself, as it assumes no scale separation. In order to do this, we follow a well-established practice in experiments: a simulation with the same parameters, same COMPASS-like diverted geometry and same particle source is carried out, using a reversed toroidal field. Conventionally, we will speak about *normal* toroidal field when the ion ∇B velocity vector points towards the divertor, while we will call the field *reversed* if the drift points upwards. This method allows to show explicitly the contribution of the $E \times B$ and the ∇B drift. The hypothesis underneath the experiments with inversion of the toroidal field, is that the drift-driven flux changes its direction while the small scale turbulence should not change its properties. The comparison of the two cases represented in figure 8 shows the main result of the simulations.

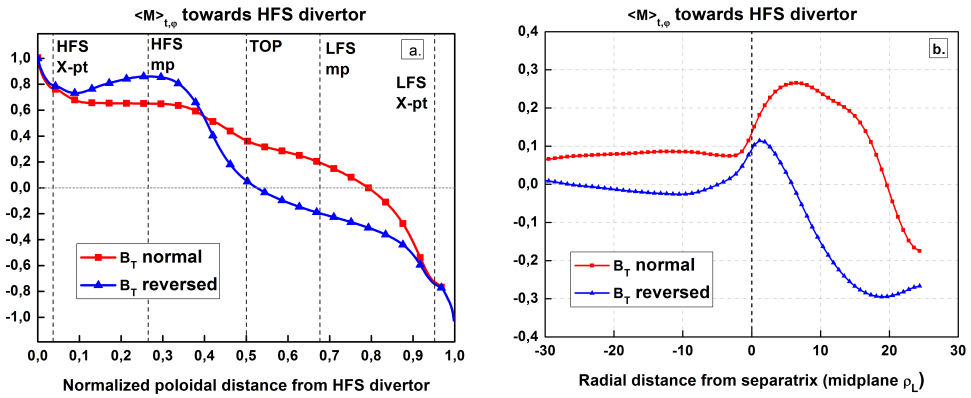

Figure 8: a) Comparison between parallel Mach numbers poloidal profiles in normal and reversed toroidal fields at $r - a = 13\ \rho_L$. b) Comparison between parallel Mach numbers radial profiles in normal and reversed toroidal fields at LFS midplane.

We notice from figure 8 that in the reversed toroidal field case the stagnation point moves upwards, positioning between the LFS midplane and the top of the machine, so at the midplane the parallel flow is reversed and directed towards the outer target. This characteristic has been found also experimentally, for example, on Alcator C-Mod and JET[1].
The radial profile at the LFS midplane shown in figure 8 is also similar to the same experiments in Alcator C-mod [30], in the case of a Greenwald density of 0.3. This qualitative agreement with experiments also in the radial direction suggests that the description of the cross-field transport of particles and momentum in the SOL is coherent, and that TOKAM3X is able to reproduce some of the main features of the complex SOL equilibrium.
In the reversed case, the transverse flux coming out from the separatrix is found to be distributed on a wider poloidal span. In fact, the inversion of the toroidal field direction has changed the direction of the ion ∇B drift, that points now upwards. In we refer to figure 6, we can understand that in the reversed field case, the source of particles is positive for the upper LFS and negative for the lower LFS. Thus, even if globally the ∇B drift is divergence-free, its local value is comparable to the $E \times B$ one and can change locally the Mach number. Also the $E \times B$ poloidal flux changes its direction, since the electric potential radial gradient in the SOL keeps its orientation. This direction inversion is another mechanism who moves the particle source for the SOL to the upper LFS. The behaviour of the radial $E \times B$ flux changes slightly. Indeed, even if the mean-field fluxes seen in figure 4 change their sign, the sum of fluctuating and turbulent fluxes is still directed outwards for the main SOL, because of the small-scale interchange turbulence. The particle source due to the radial $E \times B$ drift is still positive, and spreaded over the LFS. Globally, in the reversed field case, the particle source is concentrated in the region between the LFS midplane and the top of the machine, and so the stagnation point moves up to this region, determining a more symmetric configuration.
At the HFS midplane, the inversion of the toroidal field does not affect much the Mach number profile. At this position the parallel flow, being produced mainly by the asymmetry in the particle source in the SOL, does not change significantly with the toroidal field inversion. In the divertor region as well, the parallel Mach number is almost unchanged, at least for positions radially not too close to the separatrix, showing the prevailing effect of the solid targets on this region. This also confirms that, as pointed out in the previous sections, the cross-field transport at the separatrix in the divertor region has

a little influence on the parallel equilibrium of the SOL.
If we evaluate the poloidal asymmetry with the Mach number measured at the top of the machine, we find a difference $|\Delta M| = M_{TOP}^{norm} - M_{TOP}^{rev} \simeq 0.40$ between the cases with normal and reversed toroidal field. We can assume that, for the normal B_T case:

$$M_{TOP}^{norm} = \Delta M^{dr} + \Delta M^{turb} \tag{15}$$

Where the superscripts *dr* and *turb* are referred respectively to the contribution of the drifts and the one of turbulence. For the reversed B_T case, instead:

$$M_{TOP}^{rev} = -\Delta M^{dr} + \Delta M^{turb} \tag{16}$$

We obtain that the large-scale drifts are responsible on average for a $\Delta M^{dr} \simeq 0.2$ at the top of the machine. Since the value for the normal toroidal field is $M_{TOP}^{norm} \simeq 0.4$, also the turbulence contribution is around 0.2. From figure 8b we notice that the shift in the parallel Mach number, occurring with the toroidal field inversion, affects the majority of the SOL in its radial extension. This simulation confirms, so, that large-scale drifts and small-scale turbulence have comparable effects on the parallel flow in the SOL. This is an extremely simplified calculation to resume briefly the simulation results, but one must be aware that the overall equilibrium state of the plasma changes with the inversion of the toroidal field. Changing the poloidal equilibrium of the plasma indeed, not only changes the direction of the $E \times B$ and $\vec{\nabla} B$ drifts, but also their magnitude. Moreover, the small-scale turbulent transport is found to change its characteristics, in contrast with the hypothesis on which the experiment is based. In normal field configuration, a better confinement is observed, with the build-up of a small transport barrier at the separatrix, which is weaker in the reversed toroidal field. The overall equilibrium is changed between the two situations, with a higher density in the closed field lines for the normal field case and the formation of a small pedestal, as visible in figure 9.

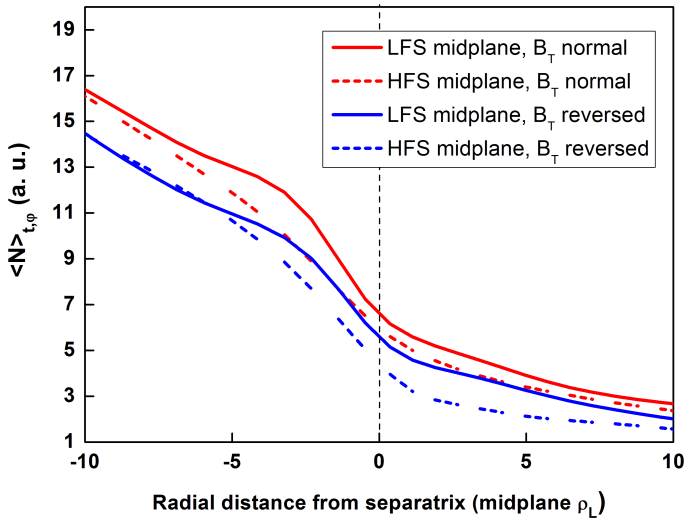

Figure 9: Average density radial profiles mapped ad the LFS midplane for the normal B_T and for the reversed B_T case.

This transport barrier could be due to the radial shear of the poloidal velocity, that is bigger in the normal case if compared to the reverse one. For the open flux surfaces indeed, below the stagnation point the poloidal $E \times B$ drift and the poloidal projection of the parallel velocity overlap constructively in a normal field configuration, while they partially cancel in the reverse field one. This situation produces a bigger radial shear in the poloidal velocity at the midplane for normal configuration. This behaviour has been found also in the experiments, and reminds of the formation of transport barriers in the H-mode confinement. A detailed analysis of the mechanism for the build up of the transport barrier is beyond the scope of the paper. Nevertheless, in our simulations the variation of turbulent transport properties appears to influence the overall equilibrium. The large-scale and small scale $E \times B$ flows do not simply superpose linearly, but they show a complex non-linear interplay. These results confirm once again the importance in the simulation of the plasma edge of an integrated approach that includes the self-consistent description of turbulent transport.

8 Conclusion

The 3D fluid turbulence code TOKAM3X has been used to tackle the problem of the poloidal asymmetries in parallel flux in the Scrape-Off Layer. For the first time, the code is run in realistic divertor magnetic configuration, in a COMPASS-like geometry. At the same time so, the code is capable to describe self-consistently the turbulence in the edge plasma, the effects related to drifts, and to explore the aspects related to the divertor geometry. This approach gives a global insight on the complex equilibrium in the edge plasma.

The main experimental features of the parallel flow in the Scrape-Off Layer are well reproduced by the code as, for example, the position of the stagnation point between the LFS X-point and the LFS midplane, and a parallel Mach number close to 0.4 at the top of the machine. The parallel Mach number profile resulting from the simulation is compared to the multi-machine measurement reported in [1]. Some of these experimental points are obtained in a high-recycling regime: the physics associated to this particular condition is not fully reproduced by the presented TOKAM3X simulations because of the isothermal assumption. Nevertheless, experimental trends are qualitatively recovered, as well as the right order of magnitude for the Mach number val-

ues in the different poloidal locations. This suggests that at least some of the fundamental physics underlying the driving of the parallel flows in the SOL is caught by the code.
A global sight on the the $E \times B$ fluxes crossing the separatrix is presented, in order to analyze the possible mechanisms driving the parallel flows. Mean-field and fluctuating contributions to the cross-field fluxes are separated a posteriori to give a hint on the relative weights of large-scale drifts and turbulence in the overall SOL equilibrium. Although the fluctuation-driven flux dominates in the vicinity of the LFS midplane, mean-field fluxes are observed to have a comparable weight. In the vicinity of the X-point, a complex $E \times B$ flux pattern caused by the particular X-point topology is found to affect the equilibrium in the first flux surfaces outside the separatrix.
The variable flux expansion, characteristic of an X-point geometry, is found to have a geometrical effect on the turbulent fluxes, which could alter the interpretation of the results. Cross-field transport organizes according to the geometry, causing higher fluxes where flux expansion is bigger, so for example at the top and near the X-point, in order to maintain the turbulent structures aligned with the field lines. In the determination of the SOL equilibrium, however, the cross-field transport is more effective when flux surfaces further out from the separatrix are reached. From this point of view, the turbulent transport causes, as expected, the main de-confinement of the plasma at the LFS midplane.
Both the divertor and the Private Flux Region appear to be turbulent. However, in our simulations, interchange turbulence is found not to be effective for cross-field transport towards the Private Flux Region. Instead, an $E \times B$ steady-state flow is observed across the separatrix, even if without a significant impact on the SOL parallel equilibrium. These results could be very sensible to the inclusion of the temperature effects and of the neutral dynamics, especially in a high-recycling regime, where magnitude and direction of the cross-field fluxes in proximity of the target could change, and different types of instabilities could appear. Nevertheless, these isothermal simulations represent a necessary basic knowledge of the turbulence properties in the divertor region that will be useful for the understanding of more complex anisothermal simulations.
Taking advantage of this global flux picture, we studied the role of $E \times B$ and ∇B fluxes for the driving of parallel fluxes in the SOL. The small-scale turbulent transport is shown to be an important source of poloidal asymmetry, but also the $E \times B$ poloidal fluxes and the ∇B drifts act as parallel flow

sources preferentially for the LFS. With this schematic view, it is possible to understand the positioning of the stagnation point in the region below the LFS midpane. A semi-analytical model is used to evaluate the steady state poloidal drift effect on poloidal asymmetries in the closed field lines region, in a non-turbulent case. A mode $m = 1$ is found for density and parallel Mach number, revealing the role of the poloidal drifts in the build-up of poloidal asymmetries. This can be captured only by solving at the same time the mass and the parallel momentum balance. Poloidal asymmetries in the SOL density for turbulent simulations are stronger than what is found in the reduced model, suggesting an important role of turbulence in the driving of the poloidal asymmetry. Nevertheless, the driving of parallel flows by the poloidal drifts discussed with this study can be seen as an underlying effect that has to be taken into account for the analysis of the turbulent simulations.

A simulation with a reversed toroidal field allows to distinguish in a self-consistent way the role of the large-scale drifts compared to the one of turbulence. In the reversed toroidal field case, a shift occurs on the parallel Mach number along the Low Field Side of the SOL, with the inversion of the parallel flux at the midplane, once again in good agreement with experiments. This is due to the inversion of the direction of the $E \times B$ poloidal drift and of the ∇B drift, which bring the majority of the parallel flow source on the upper LFS. At the same time, the in-out asymmetry is maintained by the small-scale turbulence, which changes only slightly its properties with the toroidal field inversion. Small changes are noticed on the HFS, where parallel transport seems to play a major role, and in the divertor region. This simulation confirms the comparable weight of small-scale and large-scale $E \times B$ flows in the set-up of the parallel equilibrium.

The results of our simulations show in general a complex interplay between turbulence and large-scale flows, underlining the importance of having a global approach in the simulation of the plasma edge. The analysis of this interplay will be pushed forward, in order to disentangle the various mechanisms driving the equilibrium in the edge plasma. Moreover, in a near future, neutral dynamics will be included in simulations, in order to better describe high-density regimes.

Acknowledgements

This work has been carried within the framework of EUROfusion Consortium and has received funding from the EURATOM research and training programs under grant agreement WP14/ER/CEA09. The authors would like to thank the financial support by the AMIDEX project KFC.
This work was granted access to the HPC resources of IDRIS, under the allocations i2015056912 and i20150242 made by GENCI, and of Aix-Marseille University, financed by the project Equip@Meso (ANR-10-EQPX-29-01) of the program "Investissements d' Avenir"supervised by the Agence Nationale de la Recherche (National Research Agency).
The view and opinions expressed herein do not necessarily reflect those of the European Commission.

References

[1] N. Asakura. Understanding the SOL flow in L-mode plasma on divertor tokamaks, and its influence on the plasma transport. *Journal of Nuclear Materials*, 365:41–51, 2007.

[2] R. A. Pitts, P. Andrew, X. Bonnin, A. V. Chankin, Y. Corre, G. Corrigan, D. Coster, I. Duran, T Eich, S. K. Erents, W. Fundamenski, A. Huber, S. Jachmich, G. Kirnev, M. Lehnen, P. J. Lomas, A. Loarte, G. F. Matthews, J. Rapp, C. Silva, M. F. Stamp, J. D. Strachan, and E. Tsitrone. Edge and divertor physics with reversed toroidal field in JET. *Journal of Nuclear Materials*, 339:146–153, 2005.

[3] G.S. Kirnev, G. Corrigan, D. Coster, S.K. Erents, W. Fundamenski, G.F. Matthews, and R.A. Pitts. EDGE2D code simulations of SOL flows and inout divertor asymmetries in JET. *Journal of Nuclear Materials*, 337-339:271–275, mar 2005.

[4] J. P. Gunn, C. Boucher, M. Dionne, V. Fuchs, T. Loarer, J. Sto, I. Nanobashvili, R. Pa, J. Ada, J. Bucalossi, R. Dejarnac, T. Van. Rompuy, R. Zago, P. Devynck, P. Hertout, M. Hron, G. Lebrun, P. Moreau, F. Rimini, A. Sarkissian, and G. Van. Oost. Evidence for a poloidally localized enhancement of radial transport in the scrape-off layer of the Tore Supra tokamak. *Journal of Nuclear Materials*, 365:484–490, 2007.

[5] V. Naulin, T. Windisch, and O. Grulke. Three-dimensional global fluid simulations of cylindrical magnetized plasmas. *Physics of Plasmas*, 15(1), 2008.

[6] P Ricci, F D Halpern, S Jolliet, J Loizu, A Mosetto, A Fasoli, I Furno, and C Theiler. Simulation of plasma turbulence in scrape-off layer conditions: the gbs code, simulation results and code validation. *Plasma Physics and Controlled Fusion*, 54(12):124047, 2012.

[7] J Juul Rasmussen, A H Nielsen, J Madsen, V Naulin, and G S Xu. Numerical modeling of the transition from low to high confinement in magnetically confined plasma. *Plasma Physics and Controlled Fusion*, 58(1):014031, 2016.

[8] P. Tamain, H. Bufferand, G. Ciraolo, C. Colin, E. Serre, and F. Schwander. The tokam3x code for edge turbulence fluid simulations of tokamak plasmas in versatile magnetic geometries. *Journal of Computational Physics*, Accepted for publication, 2016.

[9] N. R. Walkden, B. D. Dudson, and G. Fishpool. Characterization of 3D filament dynamics in a MAST SOL flux tube geometry. *Plasma Phys. Control. Fusion*, 55:105005, 2013.

[10] N.R. Walkden, B.D. Dudson, L Easy, G Fishpool, and J.T. Omotani. Numerical investigation of isolated filament motion in a realistic tokamak geometry. *Nucl. Fusion*, 55(11):113022, 2015.

[11] T.Y. Xia, X.Q. Xu, and P.W. Xi. Six-field two-fluid simulations of peelingballooning modes using bout++. *Nuclear Fusion*, 53(7):073009, 2013.

[12] H. Y. Guo, J. Li, B. N. Wan, X. Z. Gong, Y. F. Liang, G. S. Xu, X. D. Zhang, S. Y. Ding, K. F. Gan, J. S. Hu, L. Q. Hu, S. C. Liu, J. P. Qian, Y. W. Sun, H. Q. Wang, L. Wang, T. Y. Xia, B. J. Xiao, L. Zeng, Y. P. Zhao, P. Denner, J. R. Ferron, A. M. Garofalo, C. T. Holcomb, A. W. Hyatt, G. L. Jackson, A. Loarte, R. Maingi, J. E. Menard, M. Rack, W. M. Solomon, X. Q. Xu, M. Van Zeeland, X. L. Zou, and EAST Team. Recent advances in long-pulse high-confinement plasma operations in experimental advanced superconducting tokamaka). *Physics of Plasmas*, 21(5), 2014.

[13] T. Y. Xia and X. Q. Xu. Nonlinear fluid simulation of particle and heat fluxes during burst of elms on diii-d with bout++code. *Nuclear Fusion*, 55(11):113030, 2015.

[14] J. Loizu, P. Ricci, F. D. Halpern, S. Jolliet, and A. Mosetto. Intrinsic toroidal rotation in the scrape-off layer of tokamaks. *Physics of Plasmas*, 062309, 2014.

[15] J. Loizu, P. Ricci, F.D. Halpern, S. Jolliet, and A. Mosetto. Effect of the limiter position on the scrape-off layer width, radial electric field and intrinsic flows. *Nuclear Fusion*, 54(8):083033, 2014.

[16] C. S. Chang and S. Ku. Spontaneous rotation sources in a quiescent tokamak edge plasma. *Physics of Plasmas*, 15(6), 2008.

[17] C. Baudoin, P. Tamain, G. Ciraolo, R. Futtersack, A. Gallo, P. Ghendrih, Y. Marandet, N. Nace, and C. Norscini. On the effect of electron temperature fluctuations on turbulent heat transport in the edge plasma of tokamaks. *Contributions to Plasma Physics*, (September):6–11, 2015.

[18] P. Tamain, Ph. Ghendrih, E. Tsitrone, Y. Sarazin, X. Garbet, V. Grandgirard, J. Gunn, E. Serre, G. Ciraolo, and G. Chiavassa. 3D modelling of edge parallel flow asymmetries. *Journal of Nuclear Materials*, 390-391:347–350, jun 2009.

[19] C. Colin, P. Tamain, F. Schwander, E. Serre, H. Bufferand, G. Ciraolo, N. Fedorczak, and Ph. Ghendrih. Impact of the plasma-wall contact position on edge turbulent transport and poloidal asymmetries in 3D global turbulence simulations. *Journal of Nuclear Materials*, 463:654–658, 2015.

[20] F. L. Hinton and C. W. Horton. Amplitude Limitation of a Collisional Drift Wave Instability. *Physics of Fluids*, 14:116, 1971.

[21] P. Tamain, H. Bufferand, G. Ciraolo, C. Colin, E. Serre, and F. Schwander. 3D Properties of Edge Turbulent Transport in Full-Torus Simulations and their Impact on Poloidal Asymmetries. *Contributions to Plasma Physics*, 559(4):555–559, 2014.

[22] P. Tamain. Progress towards selfconsistent modelling of the interaction between turbulence and pwi physics in edge transport and turbulence codes. In *Proceedings of ITPA Div-SOL meeting, Princeton*, 2015.

[23] V. Weinzettl, R. Panek, M. Hron, J. Stockel, F. Zacek, J. Havlicek, P. Bilkova, D.I. Naydenkova, P. Hacek, J. Zajac, R. Dejarnac, J. Horacek, J. Adamek, J. Mlynar, F. Janky, M. Aftanas, P. Bohm, J. Brotankova, D. Sestak, I. Duran, R. Melich, D. Jares, J. Ghosh, G. Anda, G. Veres, A. Szappanos, S. Zoletnik, M. Berta, V.F. Shevchenko, R. Scannell, M. Walsh, H.W. Müller, V. Igochine, A. Silva, M. Manso, R. Gomes, Tsv. Popov, D. Sarychev, V.K. Kiselov, and S. Nanobashvili. Overview of the COMPASS diagnostics. *Fusion Engineering and Design*, 86(6-8):1227–1231, oct 2011.

[24] Ph. Ghendrih, K. Bodi, H. Bufferand, G. Chiavassa, G. Ciraolo, N. Fedorczak, L. Isoardi, A. Paredes, Y. Sarazin, E. Serre, F. Schwander, and P. Tamain. Transition to supersonic flows in the edge plasma. *Plasma Physics and Controlled Fusion*, 53(5):054019, 2011.

[25] N. Smick, B. LaBombard, and I. H. Hutchinson. Transport and drift-driven plasma flow components in the Alcator C-Mod boundary plasma. *Nuclear Fusion*, 53(2):023001, feb 2013.

[26] T. D. Rognlien, G. D. Porter, and D. D. Ryutov. Influence of E X B and gradB drift terms in 2-D edge/SOL transport simulations. *Journal of Nuclear Materials*, 269:654–659, 1999.

[27] T. Eich, A.W. Leonard, R.A. Pitts, W. Fundamenski, R.J. Goldston, T.K. Gray, A. Herrmann, A. Kirk, A. Kallenbach, O. Kardaun, A.S. Kukushkin, B. LaBombard, R. Maingi, M.A. Makowski, A. Scarabosio, B. Sieglin, J. Terry, A. Thornton, ASDEX Upgrade Team, and JET EFDA Contributors. Scaling of the tokamak near the scrape-off layer h-mode power width and implications for iter. *Nuclear Fusion*, 53(9):093031, 2013.

[28] J. R. Harrison, G. M. Fishpool, and B. D. Dudson. Filamentary transport in the private flux region in MAST. *Journal of Nuclear Materials*, 2:2–5, 2014.

[29] A. V. Chankin and P. C. Stangeby. Toroidicity in the tokamak sol: effects on poloidal asymmetries, radial current and the l - h transition. *Plasma Physics and Controlled Fusion*, 38(11):1879, 1996.

[30] B. LaBombard, J.E. Rice, A.E. Hubbard, J.W. Hughes, M. Greenwald, J. Irby, Y. Lin, B. Lipschultz, E.S. Marmar, C.S. Pitcher, N. Smick, S.M. Wolfe, S.J. Wukitch, and the Alcator Group. Transport-driven scrape-off-layer flows and the boundary conditions imposed at the magnetic separatrix in a tokamak plasma. *Nuclear Fusion*, 44(10):1047, 2004.

[31] P. C. Stangeby. *The Plasma Boundary of Magnetic Fusion Devices*. 2000.

[32] A.V Chankin, D.P Coster, N Asakura, G Corrigan, S.K Erents, W Fundamenski, H.W Müller, R.a Pitts, P.C Stangeby, and M Wischmeier. A possible role of radial electric field in driving parallel ion flow in scrape-off layer of divertor tokamaks. *Nuclear Fusion*, 47(8):762–772, 2007.